LOGO

Effective Brain Connectivity Extraction by Frequency-Domain Convergent Cross-Mapping (FDCCM) and its Application in Parkinson's Disease Classification

Sandeep Avvaru, Graduate Student Member, IEEE; and Keshab K. Parhi, Fellow, IEEE

Abstract—Objective: Inferring causal or effective connectivity between measured timeseries is crucial to understanding directed interactions in complex systems. This task is especially challenging in the brain as the underlying dynamics are not well-understood. This paper aims to introduce a novel causality measure called frequencydomain convergent cross-mapping (FDCCM) that utilizes frequency-domain dynamics through nonlinear state-space reconstruction. Method: Using synthesized chaotic timeseries, we investigate general applicability of FDCCM at different causal strengths and noise levels. We also apply our method on two resting-state Parkinson's datasets with 31 and 54 subjects, respectively. To this end, we construct causal networks, extract network features, and perform machine learning analysis to distinguish Parkinson's disease patients (PD) from age and gender-matched healthy controls (HC). Specifically, we use the FDCCM networks to compute the betweenness centrality of the network nodes, which act as features for the classification models. Result: The analysis on simulated data showed that FDCCM is resilient to additive Gaussian noise, making it suitable for real-world applications. Our proposed method also decodes scalp-EEG signals to classify the PD and HC groups with approximately 97% leave-one-subject-out cross-validation accuracy. We compared decoders from six cortical regions to find that features derived from the left temporal lobe lead to a higher classification accuracy of 84.5% compared to other regions. Moreover, when the classifier trained using FDCCM networks from one dataset was tested on an independent out-of-sample dataset, it attained an accuracy of 84%. This accuracy is significantly higher than correlational networks (45.2%) and CCM networks (54.84%). Significance: These findings suggest that our spectral-based causality measure can improve classification performance and reveal useful network biomarkers of Parkinson's disease.

Index Terms—Brain networks, convergent crossmapping, frequency-domain convergent crossmapping, classification, effective connectivity, electroencephalography, functional connectivity, machine learning, Parkinson's disease

I. INTRODUCTION

The human brain is an efficient organization of 100 billion (10^{11}) neurons anatomically connected by about 100 trillion (10^{14}) synapses over multiple scales of space and functionally interactive over multiple scales of time [1]. The

S. Avvaru and K. K. Parhi are with the Department of Electrical and Computer Engineering, University of Minnesota, Minneapolis, MN 55455, USA (email: avvar002@umn.edu and parhi@umn.edu).

This research was supported in part by the National Science Foundation under grant number CCF-1954749.

recent mathematical and conceptual development of network science combined with the technological advancement of measuring neuronal dynamics motivated the field of network neuroscience. Network science provides a particularly appropriate framework to study several mechanisms in the brain by treating neural elements (a population of neurons, a subregion) as nodes in a graph and neural interactions (synaptic connections, information flow) as its edges. The central goal of network neuroscience is to link macro-scale human brain network topology to cognitive functions and clinical disorders. It is established that neurological disorders and cognitive phenomena can be described as aberrant patterns of interactions between neural elements in a large-scale brain network [2]–[5].

Apart from the anatomical/structural connectivity, measured neural dynamics can be used to estimate functional and effective networks. While functional connectivity is defined as a statistical dependence between the neurophysiological signals, effective connectivity characterizes patterns of causal interactions [6]. While the underlying anatomical pathways between brain regions or populations of neurons are bidirectional, we cannot assume that the connectivity is symmetrical. Although there are several linear and nonlinear measures of undirected correlation, estimating the directionality in brain networks is an important and largely unaddressed issue [7]. This paper proposes a novel approach to estimate causal connectivity that can be applied to different types of electrophysiological brain recordings.

Data-driven effective connectivity measures can vary from linear to nonlinear, model-based to model-free, and time-domain to frequency-domain [8], [9]. Majority of the existing measures are based on Granger's approach [9]–[11]. However, these Granger-based measures such as Granger causality, directed transfer function (DTF), and partial directed coherence (PDC) are only applicable to strongly-coupled, linear, and stochastic systems [12], [13]. Granger causality is also model-based and does not always reveal causal interactions [13], [14].

A newly developed method of assessing causation between timeseries, convergent cross-mapping (CCM) [14], has been shown to identify causal relationships that Granger causality may miss due to nonlinearity or deterministic nature. CCM has been applied in a limited number of studies to characterize neurological disorders [15]–[18]. CCM is based on time-domain dynamics and does not include spectral information. Frequency-based methods such as PDC [19], DTF [20] and dynamic causal modeling [21] have been shown to be useful in

detecting brain disorders [22]–[26]. However, these methods are derived using Granger's approach and are model-based [27]. This paper introduces the first frequency-based causality measure that can infer nonlinear causal interactions between neuronal populations without requiring any model estimation.

The proposed method called *frequency-domain convergent cross-mapping* (FDCCM) is a nonlinear state-space reconstruction technique similar to CCM. For two causally coupled neuronal dynamics, the rationale behind causal inference using FDCCM is based on the following intuition. Since the cause-variable influences the effect-variable, we can reconstruct the causal timeseries by finding its signature in the power spectrum of the effect timeseries. In other words, we utilize the mapping between the power spectra of the two timeseries to estimate the causal influence of one on the other. We first illustrate the principle of our approach on simple synthesized data, coupled logistic maps, and show that FDCCM reliably estimates interactions. Next, we apply the method to real-world datasets and evaluate its performance in detecting biomarkers for Parkinson's disease using resting-state EEG.

The specific contributions of the paper are outlined below:

- We introduce a spectral measure of causality called frequency-domain convergent cross-mapping or FD-CCM. Unlike existing spectral measures of effective connectivity, FDCCM is model-free and can infer nonlinear interactions.
- 2) We describe the algorithm and validate our method on a synthesized dataset. We illustrate the effect of coupling strength and noise on the quality of causal inference, and demonstrate that FDCCM is more robust to external noise than CCM.
- 3) We apply our method on resting-state scalp EEG recordings from two Parkinson's datasets. We employ graph analysis to showcase the difference in betweenness centrality between the patients and controls.
- 4) We demonstrate that machine learning classifiers based on FDCCM causal networks can differentiate between Parkinson's patients and demographically matched healthy controls. The performance of FDCCM is shown to be better than correlational networks and CCM networks on both datasets.

II. DATA DESCRIPTION

Three datasets are used in this analysis. The first is a synthesized dataset that simulates nonlinear causal interactions between two variables. The second and third datasets contain experimental resting-state scalp EEG recordings from Parkinson's patients and healthy controls.

A. Synthesized Data

The logistic map is a well-established nonlinear dynamic equation that generates periodic and chaotic behavior [28]. Despite its mathematical simplicity, a logistic map exhibits a high degree of complexity. Two logistic maps with chaotic dynamics can be coupled to create a complex system akin to biological systems. Two timeseries in a coupled logistic map can be correlated, uncorrelated, or anti-correlated at different

times [14]. The coupled logistic maps timeseries X and Y were synthesized using the following equations:

$$x(t+1) = x(t)[r_x(1-x(t)) - \beta_{xy}y(t)]$$

$$y(t+1) = y(t)[r_y(1-y(t)) - \beta_{yx}x(t)].$$
(1)

The variables X and Y have a nonlinear dependence on their own past values parameterized by the growth rates r_x and r_y . The coupling constants β_{yx} and β_{xy} characterize the coupling strengths from X to Y and from Y to X, respectively. The variables have chaotic dynamics at values of r_x and r_y above 3.57. We chose the $r_x=3.65$ and $r_y=3.77$, so we are in the chaotic regime of the logistic map [29].

B. Parkinson's Data

1) Subjects: We used two Parkinson's datasets in this study. The first dataset includes EEG data from 15 PD patients (mean age 63.2 ± 8.2 years) and 16 healthy, age-matched control participants (mean age 63.5 ± 9.6 years). The PD and control groups include eight and nine females, respectively. All PD patients were diagnosed by a movement disorder specialist at Scripps Clinic in La Jolla, California. All participants provided written consent as per the Institutional Review Board of the University of California, San Diego, and the Declaration of Helsinki. Additional information about this data can be found in [30], [31].

The second dataset includes scalp EEG recordings from 27 patients with PD who were recruited from the Albuquerque, New Mexico community and an equal number of demographically matched (sex and age) controls. The PD and control groups did not differ on education or premorbid intelligence measurements. All participants were evaluated using Mini-Mental State Exam (MMSE) and achieved a score above 26. All procedures were approved by the University of New Mexico Office of the Institutional Review Board, and the participants were paid \$20/hour. The data were also reported in previous studies [32]–[34], and can be downloaded from [35].

Both datasets include data collected from PD patients in 'on medication' (PD-ON) and 'off medication' (PD-OFF) states. Data from on and off medication were collected on different days. The patients discontinued their dopaminergic medicines at least 12 hours before the experiment for the PD-OFF phase.

2) EEG Recordings: In PD dataset-1, EEG data were acquired using a 32-channel BioSemi ActiveTwo system, sampled at 512 Hz. Resting data were recorded for at least 3 min while the participants were told to fixate on a cross presented on a screen. PD dataset-2 consists of EEG signals recorded via Ag/AgCl electrodes with a sampling rate of 500 Hz on a 64-channel Brain Vision system. The signals were referenced with respect to the 'CPz' channel, resulting in 63 timeseries. This analysis considers resting-state EEG signals of one-minute duration recorded while the participants had their eyes closed (unlike PD dataset-1). The EEG channel locations in the two datasets are depicted in Fig. S1 (see Supplementary Information).

We high-pass filtered the signals at 0.5 Hz cut-off to remove low frequency drift. We also filtered all signals using a 6th order IIR filter, to remove the power-line noise and its harmonics. We used two-way (bidirectional) filtering to avoid any phase shifting that can affect causal inference between the signals.

III. METHODS

A. Convergent Cross-Mapping (CCM)

In dynamical systems, causally interacting variables (e.g., two electrode recordings) share a trajectory in the underlying state-space called 'attractor' space. In other words, each time-point corresponds to a location in this space. Mathematical theorems guarantee that the temporal sequence of a single variable has sufficient information about the entire system's dynamics. Accordingly, the dynamics of one variable constrain the dynamics of other variables, and can be used to reconstruct the original global attractor topology.

Consider two timeseries, X and Y, part of a deterministic dynamical system denoted by M. We can then express the temporal dynamics of X in a delay-coordinate state-space that consists of the set of D-dimensional state vectors: $\mathbf{x}(\mathbf{t}) = \{x(t), x(t-1), \ldots, x(t-(D-1))\}$. The time delays are assumed to be 1 for simplicity. This transformed state-space of X is called its attractor manifold M_X . This process of transforming a sequence into its delay-coordinate space is called time-delay embedding. As proven by Takens theorem [36], a general principle in dynamical systems is that the states of the global attractor M have a one-to-one mapping to the local attractors M_X and M_Y . Consequently the local attractors (also known as shadow manifolds) M_X and M_Y have a one-to-one correspondence with each other.

Based on this property, a protocol for inferring causation in complex systems was proposed by Sugihara et. al., using K-nearest-neighbor state-space reconstruction [14]. To understand the intuition behind this method, called convergent crossmapping (CCM), consider two variables X and Y with asymmetric interaction. That is, X influences Y but not vice-versa. The aim is to infer the causal interactions from observational timeseries X and Y. Since there is a causal connection from X to Y, the history of Y has information about X. In other words, a local neighborhood in M_Y corresponds to a local neighborhood in M_X . Therefore the 'cause-variable' X can be accurately reconstructed using the nearest neighbors in the shadow manifold M_Y , if and only if there is causal connection from X to Y. As the causal influence of X on the dynamics of Y increases, more information about X is encoded in the manifold M_Y constructed from a fixed number of observations of Y. This rationale acts as the basis for causal inference using CCM.

B. Frequency-Domain Convergent Cross-Mapping (FDCCM)

1) The Basic Concept: In the proposed frequency-domain convergent cross-mapping (FDCCM), we extend the idea of causal inference using nonlinear state-space reconstruction to the frequency-domain. Intuitively, any linear transformation of a manifold should preserve its topology: a corollary of random projection theory [37]. For a given frequency, Fourier

transform is a linear transformation. Hence, we can preserve the geometry by transforming the delay-coordinate space to frequency space, by computing the power spectrum of $\mathbf{x}(\mathbf{t})$. This transformation is equivalent to computing short-time Fourier transform (STFT) with pre-defined frequency bands. The time-delayed embedding in CCM is now replaced by spectrograms, such that each point in the resultant attractor manifold (M_X) is $\mathbf{x}(\mathbf{t}) = \{x_{f_1}(t), x_{f_2}(t), \dots, x_{f_D}(t))\}$, where the subscripts represent D different frequency bands of equal bandwidth. This embedding frequency space is illustrated in Fig. 1(a). Before outlining the algorithm of FDCCM, we describe two key ingredients of the method: cross-mapping and convergence.

2) Cross-Mapping in FDCCM: If X has a causal influence on Y, then, X will influence the frequency dynamics of Y. This 'imprint' of X on Y means that topology of M_Y obtained from Y can be used to estimate values of X. This estimate at a given time instant t is called the cross-map of x(t) given M_Y , and is denoted $\hat{x}(t)|M_Y$. If X and Y are causally coupled, then each point $\mathbf{x}(\mathbf{t})$ in M_X can be mapped to a unique point in M_Y [14].

To compute the cross-mapped estimates $\hat{x}(t)|M_Y$, we use simplex-projection algorithm as described by (2) and (3). We first obtain a small region around $\mathbf{y}(\mathbf{t})$, represented by its k nearest neighbors: $\{\mathbf{y_1}(\mathbf{t}),\mathbf{y_2}(\mathbf{t}),\ldots,\mathbf{y_k}(\mathbf{t})\}$. This neighborhood is then mapped to a set of points in M_X , represented as $\{\mathbf{x_1}(\mathbf{t}),\mathbf{x_2}(\mathbf{t}),\ldots,\mathbf{x_k}(\mathbf{t})\}$. To form a bounding simplex in D-dimensional space, we need $k \geq D+1$. The weighted mean of $\{\mathbf{x_1}(\mathbf{t}),\mathbf{x_2}(\mathbf{t}),\ldots,\mathbf{x_k}(\mathbf{t})\}$ provides the estimate of x(t) as shown in the equation,

$$\hat{x}(t)|M_Y = \sum_{i=1}^{D+1} w_i \mathbf{x_i}(\mathbf{t}). \tag{2}$$

The weighting w_i is based on the distance between $\mathbf{y}(\mathbf{t})$ and its i^{th} nearest neighbor $\mathbf{y_i}(\mathbf{t})$ as given by the equations,

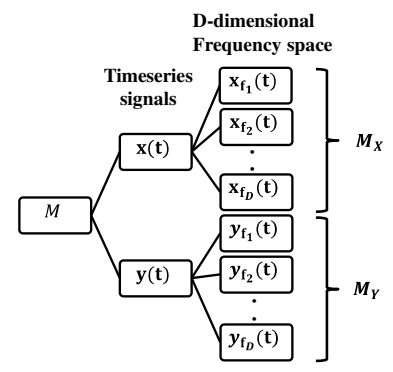
$$w_{i} = u_{i} / \sum_{j=1}^{D+1} u_{j},$$

$$u_{i} = exp \left[-\frac{d(\mathbf{y}(\mathbf{t}), \mathbf{y}_{i}(\mathbf{t})}{d(\mathbf{y}(\mathbf{t}), \mathbf{y}_{1}(\mathbf{t})} \right] \text{ and }$$

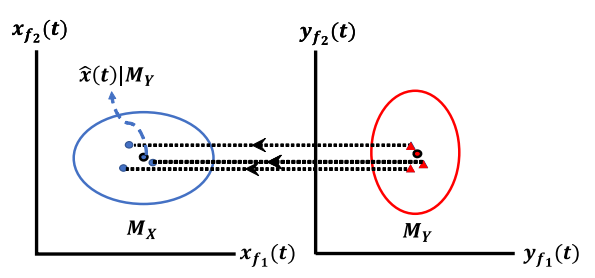
$$u_{j} = exp \left[-\frac{d(\mathbf{y}(\mathbf{t}), \mathbf{y}_{j}(\mathbf{t})}{d(\mathbf{y}(\mathbf{t}), \mathbf{y}_{1}(\mathbf{t})} \right],$$
(3)

where d(.,.) represents the Euclidean distance.

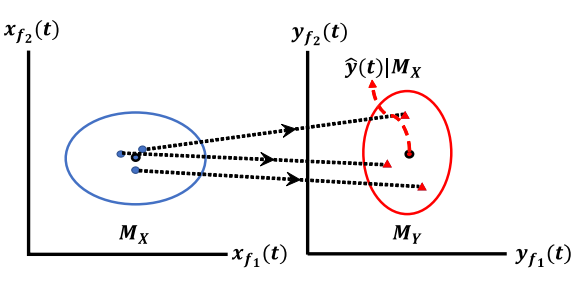
The cross-mapping was implemented for L points in the timeseries X algorithm. The total number of time points (L), i.e., the 'library' of points in the attractors used for cross-mapping is called library length. The correlation coefficient between the original timeseries and the estimated timeseries, i.e., $\rho_{\mathbf{x}\hat{\mathbf{x}}}$ is used as an indicator of the influence of X on Y. The cross-mapping $\hat{y}(t)|M_X$ can be estimated analogously. Fig. 1 illustrates the cross-mapping at time instant t for a bivariate example where X influences Y, but there is no causal link from Y to X. The state-space reconstruction of X using M_Y (i.e., $\hat{x}(t)|M_Y$) would be accurate due to the effect X has on Y, but not vice-versa.



(a) Embedding of X and Y into D frequency bands using time-frequency maps



(b) Estimating x(t) from M_Y with high accuracy



(c) Estimating y(t) from M_X with low accuracy

Fig. 1: Illustration of embedding and cross-mapping between X and Y when X influences Y but Y has no (or minimal) effect on X. Note that the cross-mapping from M_Y to M_X is accurate unlike the cross-mapping from M_X to M_Y .

- 3) Convergence: For practical application, the cross-mapping estimates of timeseries are evaluated using correlation coefficient, mean absolute error, or similar metrics. We use absolute correlation coefficient (ρ) as the accuracy metric in this study. The total number of time points, i.e., the 'library' of points in the attractors used for cross-mapping is called library length (L). As L increases, attractors get more dense in the state-space, resulting in closer nearest neighbors, and more accurate estimation. This increasing cross-mapping accuracy with increase in L is a key property for causal interactions [14]. We use the cross-mapping accuracy at L=1000. We noticed the exact value of L does not have a notable impact on the estimates unless it is assumed to be too small.
- 4) Algorithm: Here, we outline the main steps in computing FDCCM between two timeseries. For a given library length L, the basic algorithm for cross-mapping X using the shadow attractor M_Y is given by:
 - Compute the time-frequency spectrograms M_X and M_Y .

- Note that L is the number of time windows and D is the number of frequency bands.
- For each time index t = 1 to L, find D + 1 nearest neighbors of $\mathbf{y}(\mathbf{t})$ in M_Y .
- Generate weights w_i according to (3).
- Estimate $\hat{x}(t)|M_Y$ using (2).
- Calculate the absolute correlation coefficient $\rho_{\hat{X}|M_Y}$ between $X=\{x(t): 1\leq t\leq L\}$ and $\hat{X}=\{\hat{x}(t)|M_Y: 1\leq t\leq L\}$.

C. Parkinson's Classification

1) Network Features: The analysis for Parkinson's data consists of three steps: construct networks, compute node centrality of every node in the network, and learn HC vs. PD classifiers using the node centralities as features. Each of these steps is described below.

First, we construct networks using thirty-second epochs of the EEG signals. We split the recordings into multiple thirty-second epochs with 90% overlap. Since each subject PD dataset-1 has signals of duration three minutes, there are 51 such epochs per subject leading to 51 networks. In the case of PD dataset-2, the one-minute recordings produce 11 networks. Note that each recording is 3 minutes and 1 minute in dataset-1 and dataset-2, respectively. The average of these networks defines the resting-state connectivity for each subject. Each network was estimated using three network measures: correlation coefficient, CCM (time-domain) and FDCCM.

To construct networks using FDCCM, we determine the spectrograms (time-frequency matrices) for each EEG recording. Fig. 2 presents spectrograms associated with two different electrodes from a PD patient in PD dataset-1. To generate the spectrograms, we compute power spectrum with 0.5-second sliding windows with 95% overlap. The frequency resolution used was 5 Hz, up to 200 Hz. We use information up to 200 Hz as they attained better results empirically (see Table S5 in the supplementary Information). High frequency bands such as broadband gamma (50-150 Hz) activity in scalp EEG have been shown to detect biomarkers of Parkinson's in previous studies [38]–[40]. These spectrograms are then used to estimate the causal connectivity between all pairs of channels.

Thus, each healthy control subject has a representative functional or effective connectivity graph. Each PD patient has two graphs (on and off medication). We then compute betweenness centrality of the nodes in these graphs. For a subject with N channels, effective networks can have up to N(N-1) connections. That is, 992 connections if N=32, and 3906 connections if N=63. Node centrality is a way to extract interpretable information from the networks, while reducing the number of features. Betweenness centrality measures the extent to which a given node falls in the shortest path between any two other nodes [6]. Therefore, it is a measure of importance of the node acting as a bridge between other nodes in the graph.

2) Channel-Level Feature Selection and Classification: We train separate classifiers to differentiate PD-ON and PD-OFF

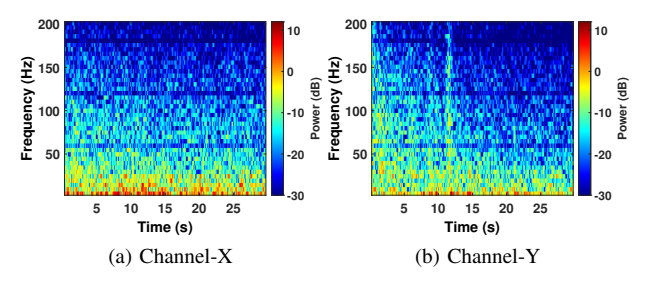


Fig. 2: Example time-frequency representations (spectrogram) derived from two arbitrarily chosen channels. The spectrograms correspond to a Parkinson's patient from PD dataset-1. Time resolution: 0.5-second windows with 95% overlap. Frequency resolution: 5Hz, up to 200 Hz.

from controls. Betweenness centrality of the nodes in each network are used as features. Sequential forward selection was employed to select the optimal features/channels that maximize leave-one-subject-out cross-validation accuracy. We employ Naive Bayes classifiers with Gaussian kernels which learns a nonlinear decision boundary between the two classes. We observed that these models perform better than other linear models such as support-vector machines (SVM) and linear discriminant analysis; and nonlinear models such as polynomial SVM and decision trees (see Tables S1 – S4 in the Supplementary Information). The cross-validation prevents overestimating the accuracy due to over-fitting of training data and ensures the models were evaluated on all subjects.

3) Region-Level Classification: We perform further analysis by merging the channels into six regions: frontal, central, parietal, occipital, left temporal, and right temporal, as depicted in Fig. 3. In each region, we average the betweenness centrality features of the corresponding channels. This merging of features into six regions served as a way to consolidate and reduce the number of features, thereby eliminating the need for additional feature selection. We then train separate classifiers (decision trees) for each region using the resultant averaged betweenness centrality. We evaluate these classifiers on independent 'in-sample' and 'out-of-sample' test sets and compare the performance of the six brain regions.

IV. RESULTS

A. Synthesized Data Analysis

1) Convergence: We synthesized coupled logistic maps, X and Y, using (1) with parameters: $r_x=3.65, r_y=3.77, \beta_{xy}=0.05,$ and $\beta_{yx}=0.5.$ 25,000 samples were generated and the first 10,000 were discarded to avoid the effects of transient behaviour of the model. The remaining 15,000 points were used for the analysis, assuming a 500 Hz sampling rate — a total duration of thirty seconds. To estimate spectrograms and FDCCM, we used a 5Hz frequency resolution, up to 200 Hz, analogous to the Parkinson's data. Fig. 4 illustrates how the cross-mapping accuracy between X and Y grows with increasing library length X. The increasing trend of Y grows with increasing library length Y and Y to Y and Y to Y, respectively. It can be observed that the

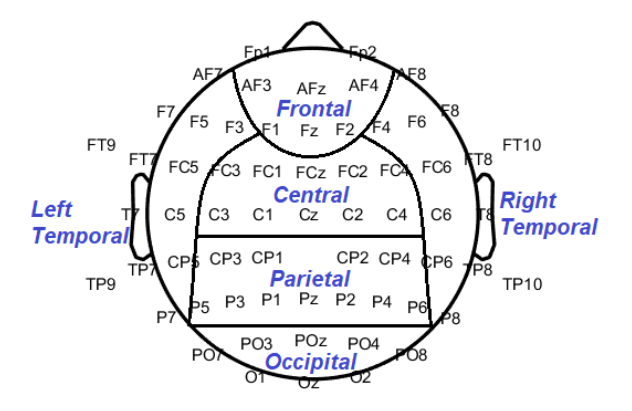


Fig. 3: EEG channels divided into six regions over scalp as frontal, central, parietal, occipital, right temporal and left temporal.

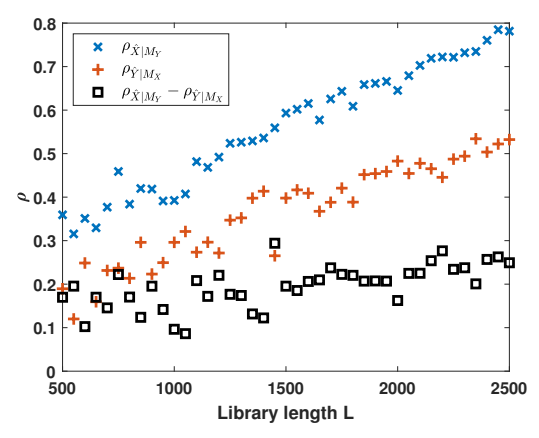


Fig. 4: Correlation coefficients of the two estimated timeseries, $\hat{X}|M_Y$ and $\hat{Y}|M_X$, with respect to library length (L). Coupling strengths: $\beta_{xy}=0.05$ and $\beta_{yx}=0.5$. $\hat{X}|M_Y$ represents the influence $X\to Y$, and $\hat{Y}|M_X$ represents the influence $Y\to X$ computed using FDCCM.

difference $\rho_{\hat{X}|M_Y}-\rho_{\hat{Y}|M_X}$ is always positive, supporting the fact that $\beta_{yx}>\beta_{xy}$.

- 2) Effect of Coupling Strength: We denote the difference $\rho_{\hat{X}|M_Y} \rho_{\hat{Y}|M_X}$ by ρ_{diff} , which is a measure of relative causal influence from X to Y. To test how the relative causality varies with coupling strength, we fix β_{xy} at 0.5, and estimate ρ_{diff} at different values of β_{yx} . Fig. 5 demonstrates that ρ_{diff} increases with increasing β_{yx} . More importantly, when $\beta_{yx} < 0.5 = \beta_{xy}$, ρ_{diff} is negative. Each value in the plot is the average result of 100 simulations. Although the direction of causality is correct, the magnitude of causal strength is not reliable when there is weak coupling. Note that there is a monotonous increase in ρ_{diff} only for coupling strengths higher than 0.35.
- 3) Effect of Noise: Since real-world signals such as electrophysiological data are affected by environmental and measurement noise, it is important to study the effect of noise. It is known that cross-mapped estimates of CCM deteriorate as more noise is present in the data [14], [29]. To characterize the effect of noise on FDCCM, we simulate noisy timeseries

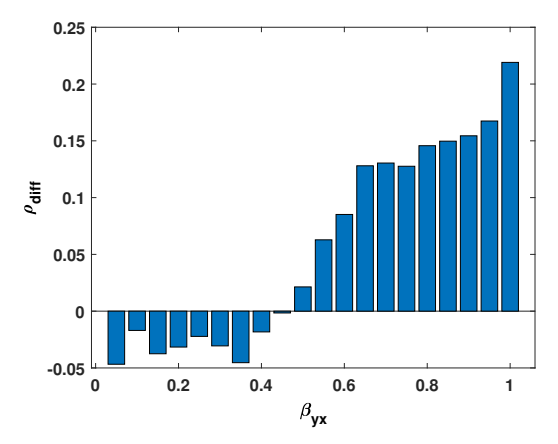


Fig. 5: Difference between $\rho_{X\to Y}$ and $\rho_{Y\to X}$ (denoted by ρ_{diff}) as a function of coupling strength β_{yx} . $\beta_{xy} = 0.5$.

given by the equations,

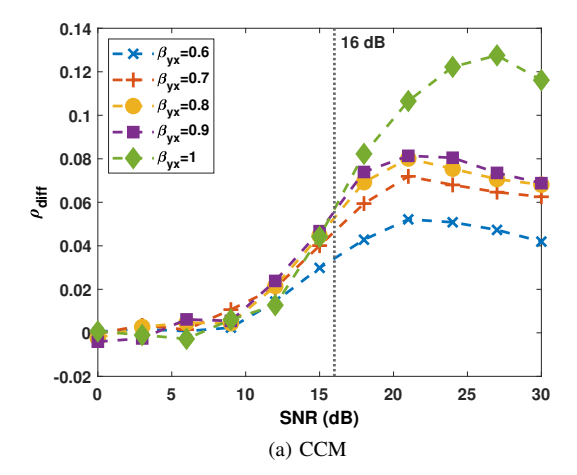
$$x(t+1) = x(t)[r_x(1-x(t)) - \beta_{xy}y(t)] + \epsilon_x(t) y(t+1) = y(t)[r_y(1-y(t)) - \beta_{yx}x(t)] + \epsilon_y(t).$$
(4)

Here, ϵ_x and ϵ_y are the noise terms, that were modeled as additive Gaussian noise with zero mean and standard deviation σ . We repeated the simulations at different signal-to-noise ratios (SNR), and different coupling strengths $\beta_{yx} = \{0.6, 0.7, 0.8, 0.9\}$. Note that β_{xy} was kept constant 0.5. We evaluated (time-domain) CCM and FDCCM by quantifying the effect of noise level on ρ_{diff} . This effect of noise on CCM and FDCCM is presented in Fig. 6.

For $\beta_{yx} > 0.5$, we expect $\rho_{diff} > 0$, as demonstrated in Fig. 1. Additionally, we expect ρ_{diff} to be higher for higher values of β_{yx} as the influence of X on Y becomes stronger. When the noise is high, i.e., SNR is zero (dB), the two timeseries become uncorrelated resulting in $\rho_{diff} = 0$. As the SNR increases, and the signal tends to dominate the noise, we notice that ρ_{diff} converges to more accurate values that are greater than zero. We can observe that both methods showcase the expected trend at high SNR: $\rho_{diff} \propto \beta_{ux}$. However, empirical data often contains a moderate level of noise. It is, therefore, important to determine the threshold at which the methods become unreliable. As shown in Fig. 6(a), when the SNR is less than 16 dB, CCM does not perform as expected at different coupling strengths. Fig. 6(b) shows that as long as the SNR is not too low, i.e., for SNR ≥ 3 dB FDCCM results in reliable estimates of ρ_{diff} . These plots illustrate that FDCCM is more robust to noise.

B. Parkinson's Disease Classification

We employ three network connectivity measures: functional (correlational) networks based on Pearson's correlation coefficient, and effective (causal) networks based on CCM and FDCCM. We compare the three methods by evaluating their performance in differentiating PD patients from healthy controls. We report the receiver operation characteristic (ROC) curves for the classifiers based on the three network types and compared them. The ROC curves plot true-positive rates vs.



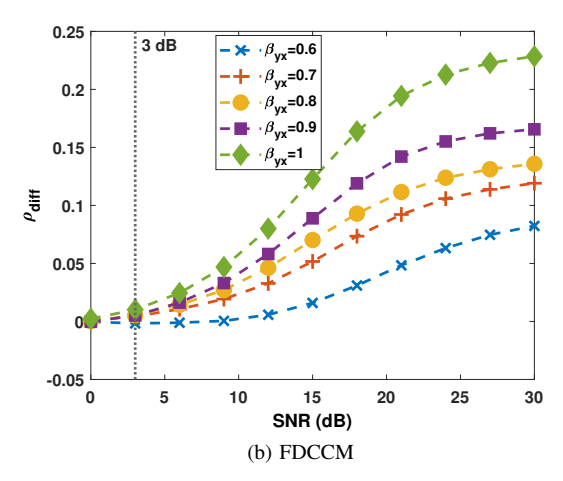


Fig. 6: The effect of noise on CCM and FDCCM estimates. ρ_{diff} as a function of increasing signal-to-noise ratio (SNR) for different coupling strengths β_{yx} .

false-positive rates for a given binary classifier at different model thresholds. As classifiers attain higher true-positive rates and lower false-positive rates, the curve moves closer to the top-left corner of the plot. In other words, classifiers that lean more towards the top-left corner of the ROC plot are more desirable.

1) Using Channel-Level Features: Betweenness centrality of the nodes in each network are used as features. Fig. 7 and Fig. 8 illustrate this distinction between patients and healthy agematched controls on the two independent resting-state datasets. The scalp topographical maps of average betweenness centrality in each group— HC, PD-ON and PD-OFF— show that the spatial distribution of betweenness centrality vary between the HC and PD groups. The HC controls have higher node centrality in the mid-frontal regions while, the PD groups show higher values in mid-parietal regions. Note that these scalp maps are derived from FDCCM networks.

The differences visualized in Fig. 7 and Fig. 8 were qualified using classifiers. Fig. 9 and Fig. 10 present the accuracy of theses classifiers in the form of ROC curves for PD dataset-1 and PD dataset-2, respectively, for all three network measures. We also report the leave-one-patient-out cross-validation ac-

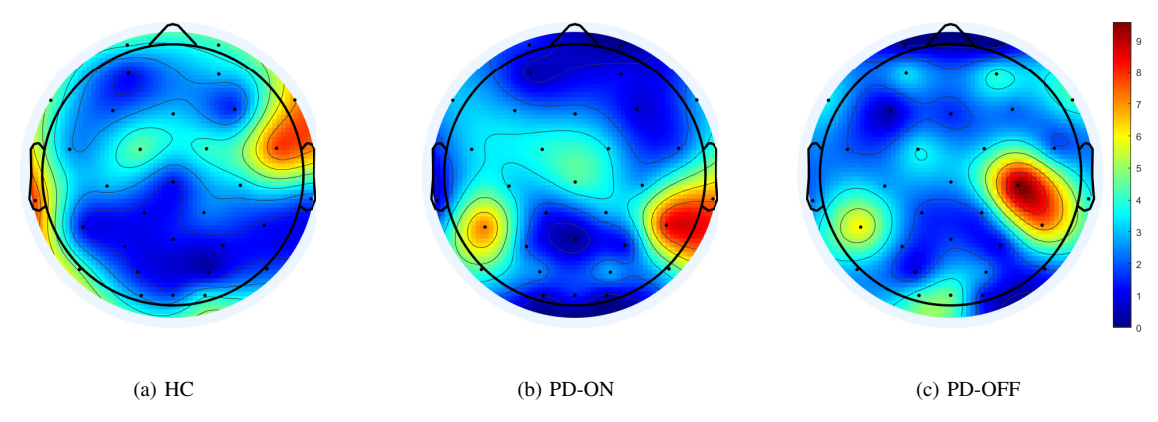


Fig. 7: Scalp topographical maps of average betweenness centralities of healthy controls (HC) and PD patients (ON and OFF) from PD dataset-1.

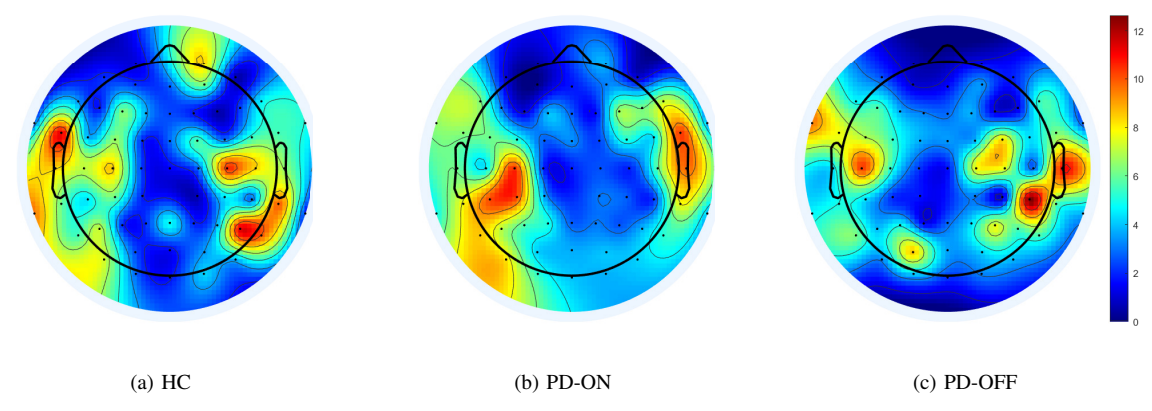


Fig. 8: Scalp topographical maps of average betweenness centralities of healthy controls (HC) and PD patients (ON and OFF) from PD dataset-2.

curacy, sensitivity and specificity of the models in Table I. The ROC curves show that FDCCM outperforms the CCM and correlation as the preferred connectivity measure, which is also indicated by higher AUC values in Table I. In PD dataset-1, FDCCM-based decoders can distinguish PD patients (both on and off medication) with 96.8% accuracy (AUC=0.98): a substantial improvement over the other two methods. Note that these decoders are based on sequential feature selection that maximizes the cross-validation accuracy. The optimal features selected by the feature selection process correspond to EEG electrodes F7 and PO4, for HC vs. PD-ON; and CP5, O1, and Oz, for HC vs. PD-OFF. The optimal features and the decoding performance vary depending on the connectivity measure used. In PD dataset-2, FDCCM achieves 96.23% accuracy (AUC=0.96) and 88.68% accuracy (AUC=0.92) for HC vs. PD-ON and HC vs. PD-OFF, respectively.

2) Using Region-Level Features: For region-level analysis, we combined both datasets to increase the size of the data. We evaluate the classifiers using 'in-sample' and 'out-of-sample' testing. In the first approach, we train the models using the features from both datasets and evaluate them using leave-one-subject-out testing. In the second approach (out-of-sample testing), we train the models using dataset-2 (since it has more subjects) and test on dataset-1. We also observed that

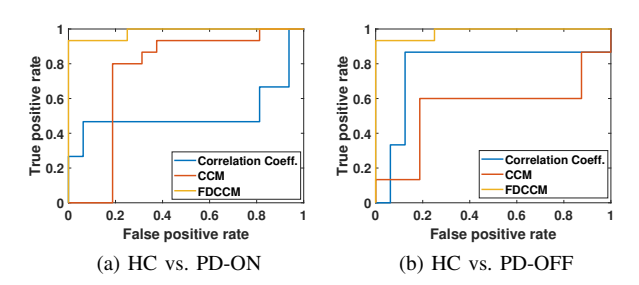


Fig. 9: HC vs. PD classification receiver operating characteristic (ROC) curves - PD dataset-1.

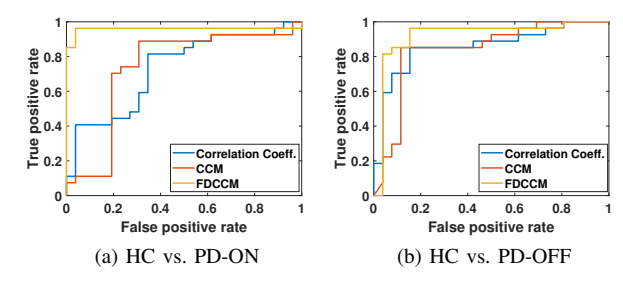


Fig. 10: HC vs. PD classification receiver operating characteristic (ROC) curves - PD dataset-2.

TABLE I: Summary of HC vs. PD channel-level validation results evaluated using leave-one-patient-out cross-validation scheme. The table presents classification accuracy, sensitivity (PD accuracy), specificity (HC accuracy) and AUC for each of the three network construction methods. Random label-assignment would result in a baseline accuracy of 50%. The highest values between the three methods are shown in bold.

	PD Dataset-1 from UCSD. $N_{PD} = 16$ and $N_{HC} = 15$														
Classifier \rightarrow	HC vs. PD-ON					HC vs. PD-OFF									
Connectivity ↓	Acc.	Acc. Sens. Spec. AUC (0-1) Selected Channels			Selected Channels	Acc.	Sens.	Spec.	AUC (0-1)	Selected Channels					
Correlation	70.97	46.67	93.7	0.51	CP1	87.1	86.67	87.5	0.78	C3, Oz					
CCM	80.64	80	81.25	0.75	FC1, O1	70.97	60	81.25	0.55	P3, Pz					
FDCCM	96.8	93.3	100	0.98	F7, PO4	96.8	93.3	100	0.98	CP5, O1, Oz					
				PD Dataset	-2 from UNM. N_P	D = 2	7 and 1	N_{HC} =	= 27						
Correlation	71.7	81.48	61.54	0.73	FC1, CP1	84.91	85.18	84.62	0.86	FC1, P7, CP2, AF7					
CCM	79.24	88.89	69.23	0.745	FC2, PO3	86.79	85.18	88.46	0.84	FT9,C3,P4,FC2,AF7,PO4,P6					
	96.23				CP1, Oz, FCz, C5				0.92	FC1, TP9, F4, P2					

HC = Healthy controls, PD = Parkinson's disease, Acc. = Accuracy, Sens. = Sensitivity, Spec. = Specificity, AUC = Area under the ROC curve.

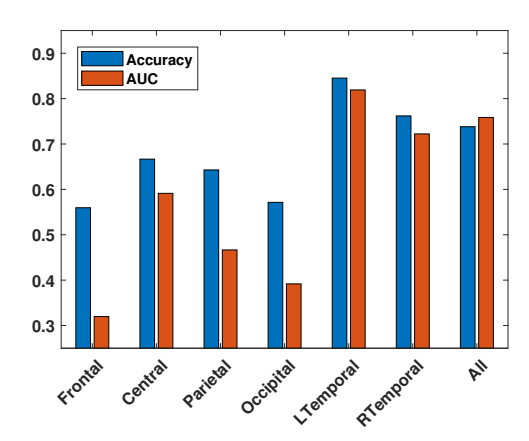


Fig. 11: Comparison of HC vs. PD classification between the six regions.

the average of the features from PD-ON and PD-OFF, i.e., (PD-ON + PD-OFF)/2, differentiates the two classes better than just PD-ON or PD-OFF.

In Fig. 11, we present the leave-one-subject-out classification accuracy using the data from both datasets based on FDCCM. The results show that the average betweenness centrality of the temporal lobe channels, especially the left temporal lobe, distinguishes PD patients with higher accuracy. The accuracy using all six features is 73.8% (AUC=0.76). However, using features from the left temporal lobe results in a substantially higher accuracy of 84.5% (AUC=0.82), followed by the right temporal lobe (Acc.=76.2% and AUC=0.72). We also observed that temporal lobe features outperformed the other regions in individual datasets.

We also compared the three connectivity measures using features from the left-temporal lobe. Table II presents the insample testing results from dataset-1, dataset-2 and combined data. In all three cases, it can be observed that FDCCM outperforms correlation and CCM. For in-sample leave-one-out testing on the combined dataset, the FDCCM networks resulted in 84.52% (AUC=0.82) accuracy, while correlational networks and CCM networks result in 63.1% (AUC=0.52) and 51.2% (AUC=0.44), respectively. For out-of-sample testing of classifiers trained on dataset-2 and tested on dataset-1, FDCCM networks lead to 83.9% accuracy, a substantial improvement

over correlational networks (Acc.=45.16%, and AUC=0.44) and CCM networks (Acc.=54.8%, and AUC=0.51).

V. DISCUSSION

A. Implications for Causal Network Analysis

Graph theory offers a powerful framework for detecting, tracking, and predicting patterns of disease in brain disorders [2], [41]. The clinical application of brain network analysis confirms that pathological patterns accumulate in network hubs and their spread/neurodegeneration are constrained by the network topology. Identifying dysfunctional brain circuits can aid in diagnosis and help improve therapeutic efficacy of invasive and noninvasive brain stimulation therapies. In particular, therapeutic efficacy is critically related to the connectivity of its target site or target brain region [42]. Although interactions between any two neural elements are inherently asymmetrical, there are relatively few techniques characterizing directional/causal connectivity. Moreover, the existing methods are limited by model assumptions.

True causality is often difficult to estimate from a model or a set of equations because one's intuitive understanding of causality becomes inherently constrained when one tries to build a model. The heterogeneity of neural interactions makes it difficult to determine a unifying causal model. There are two distinct ways (at the least) to define causality [21]. First, in terms of time-precedence, i.e., causes precede their effects: the intuition behind Granger's prediction [10]. Second, in terms of physical influence/control, i.e., changing one (the cause) changes the other (the effect). In this paper, we adopt the latter definition, and develop a state-space reconstruction technique that infers causality using the spectral dynamics of electrophysiological recordings. Our method is based on the rationale used in convergent cross-mapping (CCM) to infer dynamic causality, as introduced by Sugihara in [14]. While CCM relies on time-delay embedding a timeseries into a higher dimensional space, the proposed method, FDCCM, incorporates spectral information through time-frequency embedding of timeseries. By using power spectra instead of raw time-domain data, FDCCM blurs the effect of noise as illustrated in Fig. 6. Thus, FDCCM overcomes a prominent weakness of CCM [29].

TABLE II: Summary of HC vs. PD region-level classification results evaluated using leave-one-patient-out testing and out-of-sample testing. All classifiers were trained using left-temporal lobe features. The table presents classification accuracy, sensitivity (PD accuracy), specificity (HC accuracy) and AUC for each of the three network construction methods. Random label-assignment would result in a baseline accuracy of 50%. The highest values between the three methods are shown in bold.

		Leave-one-subject-out testing											0	ut-of-s	ample	testing
Dataset \rightarrow	PD Dataset-1			PD Dataset-2			Both Datasets				Test Set = Dataset-1					
Connectivity ↓	Acc.	Sens.	Spec.	AUC (0-1)	Acc.	Sens.	Spec.	AUC(0-1)	Acc.	Sens.	Spec.	AUC(0-1)	Acc.	Sens.	Spec.	AUC(0-1)
Correlation	51.61	46.67	56.25	0.43	64.15	59.26	69.23	0.62	63.10	57.14	69.05	0.52	45.16	0	87.5	0.44
CCM	58.06	46.67	68.75	0.45	60.38	62.96	57.69	0.52	51.19	50.00	52.38	0.44	54.84	13.33	93.75	0.51
FDCCM	80.65	73.33	87.50	0.69	79.25	81.48	76.92	0.78	84.52	90.48	78.57	0.82	83.87	86.67	81.25	0.85

HC = Healthy controls, PD = Parkinson's disease, Acc. = Accuracy, Sens. = Sensitivity, Spec. = Specificity, AUC = Area under the ROC curve.

B. Implications for Parkinson's Research

Most PD patients develop dementia in 15-20 years. Accuracy of existing clinical diagnosis of PD is only about 80% and has not improved in the last 30 years [43]. Existing studies on Parkinson's were either limited to functional magnetic resonance imaging (fMRI) data [44]–[47], or focused on spectral features [32], [48]–[51]. However, these approaches do not consider simultaneous interactions between multiple brain areas. We believe that network analysis may hold the key to identify biomarkers for early diagnosis, monitor disease progression, and establish efficacious therapies.

Modern neuroscience has shown that human brain networks exhibit high levels of clustering, a pattern indicative of a small-world architecture [52], [53]. In other words, some nodes (hub nodes) play a more important role in information transfer between different regions. This node importance can be measured using node centrality metrics such as betweenness centrality. Modulated betweenness centrality has been implicated in a wide variety of neurological disorders such as Alzheimer's, Schizophrenia and Epilepsy [2], [54]–[56]. Some prior studies on PD also showed an altered hub organization between PD and HC subjects. In particular, they showed that important nodes, i.e., nodes with higher betweenness centrality, lost significance and the nodes with a less central role have become more important [5], [57]–[59].

We quantify these changes in node centrality by building classifiers that accurately differentiate the two groups. Classifiers that use the proposed connectivity metric, i.e., FDCCM networks, consistently outperformed correlational networks and CCM networks as shown in Tables I and II. We further perform a region-wise comparison by averaging the network features in each brain region. The comparison demonstrated that temporal lobe features have a higher discriminating power. It has been shown in [60] that PD patients exhibit a decreased causal connectivity between the substantia nigra and the temporal lobe, which may explain our findings. Prior studies have also reported a link between Parkinson's disease and grey matter atrophy in the temporal lobe [61]. The proposed connectivity method, FDCCM, also aids in differentiating PD patients from healthy controls in a transfer learning setup, where the classifiers trained on one dataset are tested on an independent dataset. Our results indicate that FDCCM can detect the underlying network patterns associated with the neuropathological mechanisms of PD better than existing connectivity measures.

C. Limitations and Future Directions

There is no universal model or metric to infer causality in complex networks such as the brain. Hence, it is helpful to be aware of the shortcomings of choosing a method for a given problem. As observed from Fig. 5, FDCCM may not be reliable at low coupling strengths; this lack of reliability at certain coupling strengths is also an issue with CCM [29]. In the current form FDCCM is a bi-variate measure of relative causality. Further research is required to extend it to a multivariate measure, that can infer the causal effect between more than one timeseries, e.g., multiple channels in a brain region [18], [62].

The neural activity analyzed here was recorded from the scalp, which is affected by confounding factors such as volume conduction [63]. Also, compared to fMRI, EEG has a lower spatial resolution, making it difficult to localize the source of the activity. Table I shows that the optimal EEG channels selected by our algorithm can change depending on the classification problem and the connectivity metric used. Additionally, it can be observed that there are some differences in the scalp topographical maps between dataset-1 and dataset-2 (see Fig. 7 and Fig. 8). These differences may be attributed to the difference in the number of electrodes between the two datasets. As brain network estimation depends on the electrode density [64], it is ideal to use a higher density EEG montage (128 or 256 channels) to obtain accurate brain networks. Future research can be focused on network analysis of source-localized EEG signals or invasive recordings such as local field potentials to gain more insight into the underlying neural mechanisms of PD. A benefit of using EEG is that it can sample neural activity at 100–1000x higher time resolution than fMRI, making it more suitable to assess temporal dynamics. While more research is necessary to develop clinically applicable decoders for PD diagnosis, our work indicates that FDCCM characterizes separability between PD patients and controls.

VI. CONCLUSION

In conclusion, this study provides a novel strategy for constructing causal networks by utilizing the spectral dynamics of electrophysiological signals. We showed that our method could be applied to recognize altered network patterns in patients with PD. We conducted graph analysis and classification analysis, and demonstrated that FDCCM helps quantify these changes between patients and healthy controls. Given its excellent classification performance in distinguishing between

healthy individuals and PD patients, FDCCM could detect abnormalities and track disease progression using EEG signals. These decoders, in combination with graph theory, can also be used to develop interventional therapies such as adaptive deepbrain stimulation or transcranial direct-current stimulation [65]. Due to its non-invasiveness and wide availability, scalp EEG is also optimal for clinical, commercial, and research purposes. Further research on causal connectivity of cortical activity and comparison with source-level connectivity can help understand the underlying pathophysiology of neurodegenerative and neuropsychiatric disorders.

REFERENCES

- A. Fornito, A. Zalesky, and E. T. Bullmore, Eds., Chapter 1 An Introduction to Brain Networks. San Diego: Academic Press, 2016.
- [2] C. J. Stam, "Modern network science of neurological disorders," *Nature Reviews Neuroscience*, vol. 15, no. 10, pp. 683–695, 2014.
- [3] B. Sen, G. A. Bernstein, B. A. Mueller, K. R. Cullen, and K. K. Parhi, "Sub-graph entropy based network approaches for classifying adolescent obsessive-compulsive disorder from resting-state functional MRI," *NeuroImage: Clinical*, vol. 26, p. 102208, 2020.
- [4] T. Xu, K. R. Cullen, B. Mueller, M. W. Schreiner, K. O. Lim, S. C. Schulz, and K. K. Parhi, "Network analysis of functional brain connectivity in borderline personality disorder using resting-state fMRI," *NeuroImage: Clinical*, vol. 11, pp. 302–315, 2016.
- [5] S. Avvaru and K. K. Parhi, "Betweenness centrality in resting-state functional networks distinguishes parkinson's disease," in 44rd Annual International Conference of the IEEE Engineering in Medicine and Biology Society (EMBC), July 11th – 15th 2022.
- [6] M. Rubinov and O. Sporns, "Complex network measures of brain connectivity: Uses and interpretations," *NeuroImage*, vol. 52, no. 3, pp. 1059 – 1069, 2010, computational Models of the Brain.
- [7] V. Sakkalis, "Review of advanced techniques for the estimation of brain connectivity measured with EEG/MEG," Computers in Biology and Medicine, vol. 41, no. 12, pp. 1110–1117, 2011, special Issue on Techniques for Measuring Brain Connectivity.
- [8] J. Cao, Y. Zhao, X. Shan, H.-l. Wei, Y. Guo, L. Chen, J. A. Erkoyuncu, and P. G. Sarrigiannis, "Brain functional and effective connectivity based on electroencephalography recordings: A review," *Human Brain Mapping*, vol. 43, no. 2, pp. 860–879, 2022.
- [9] H. Bakhshayesh, S. P. Fitzgibbon, A. S. Janani, T. S. Grummett, and K. J. Pope, "Detecting connectivity in EEG: A comparative study of data-driven effective connectivity measures," *Computers in Biology and Medicine*, vol. 111, p. 103329, 2019. [Online]. Available: http://www.sciencedirect.com/science/article/pii/S0010482519301982
- [10] C. W. J. Granger, "Investigating causal relations by econometric models and cross-spectral methods," *Econometrica*, vol. 37, no. 3, pp. 424–438, 1969. [Online]. Available: http://www.jstor.org/stable/1912791
- [11] S. L. Bressler and A. K. Seth, "Wiener-granger causality:

 A well established methodology," *NeuroImage*, vol. 58, no. 2, pp. 323 329, 2011. [Online]. Available: http://www.sciencedirect.com/science/article/pii/S1053811910002272
- [12] P. A. Stokes and P. L. Purdon, "A study of problems encountered in granger causality analysis from a neuroscience perspective," *Proceedings* of the National Academy of Sciences, vol. 114, no. 34, pp. E7063–E7072, 2017. [Online]. Available: https://www.pnas.org/content/114/34/E7063
- [13] M. Cohen, Analyzing Neural Time Series Data. MIT Press, 2004.
- [14] G. Sugihara, R. May, H. Ye, C.-h. Hsieh, E. Deyle, M. Fogarty, and S. Munch, "Detecting causality in complex ecosystems," *Science*, vol. 338, no. 6106, pp. 496–500, 2012.
- [15] K. Schiecke, B. Pester, D. Piper, M. Feucht, F. Benninger, H. Witte, and L. Leistritz, "Advanced nonlinear approach to quantify directed interactions within eeg activity of children with temporal lobe epilepsy in their time course," *EPJ Nonlinear Biomedical Physics*, vol. 5, p. 3, 2017.
- [16] C. Beauchene, S. Roy, R. Moran, A. Leonessa, and N. Abaid, "Comparing brain connectivity metrics: a didactic tutorial with a toy model and experimental data," *Journal of Neural Engineering*, vol. 15, no. 5, p. 056031, 2018.
- [17] S. Avvaru, N. Peled, N. R. Provenza, A. S. Widge, and K. K. Parhi, "Region-level functional and effective network analysis of human brain during cognitive task engagement," *IEEE Transactions on Neural Sys*tems and Rehabilitation Engineering, vol. 29, pp. 1651–1660, 2021.

- [18] J. McBride, X. Zhao, N. Munro, G. Jicha, F. Schmitt, R. Kryscio, C. Smith, and Y. Jiang, "Sugihara causality analysis of scalp EEG for detection of early alzheimer's disease," *NeuroImage. Clinical*, vol. 7, pp. 258–65, 12 2015.
- [19] L. A. Baccalá and K. Sameshima, "Partial directed coherence: a new concept in neural structure determination," *Biological cybernetics*, vol. 84, no. 6, pp. 463–474, 2001.
- [20] M. Kamiński, M. Ding, W. A. Truccolo, and S. L. Bressler, "Evaluating causal relations in neural systems: Granger causality, directed transfer function and statistical assessment of significance," *Biological cybernetics*, vol. 85, no. 2, pp. 145–157, 2001.
- [21] P. A. Valdes-Sosa, A. Roebroeck, J. Daunizeau, and K. Friston, "Effective connectivity: Influence, causality and biophysical modeling," *NeuroImage*, vol. 58, no. 2, pp. 339 – 361, 2011. [Online]. Available: http://www.sciencedirect.com/science/article/pii/S1053811911003375
- [22] A. Saeedi, M. Saeedi, A. Maghsoudi, and A. Shalbaf, "Major depressive disorder diagnosis based on effective connectivity in EEG signals: A convolutional neural network and long short-term memory approach," *Cognitive Neurodynamics*, vol. 15, no. 2, pp. 239–252, 2021.
- [23] D. Wang, D. Ren, K. Li, Y. Feng, D. Ma, X. Yan, and G. Wang, "Epileptic seizure detection in long-term EEG recordings by using wavelet-based directed transfer function," *IEEE Transactions on Biomedical Engineering*, vol. 65, no. 11, pp. 2591–2599, 2018.
- [24] Y. Lu, L. Yang, G. A. Worrell, and B. He, "Seizure source imaging by means of fine spatio-temporal dipole localization and directed transfer function in partial epilepsy patients," *Clinical Neurophysiology*, vol. 123, no. 7, pp. 1275–1283, 2012.
- [25] A. P. S. de Oliveira, M. A. de Santana, M. K. S. Andrade, J. C. Gomes, M. C. Rodrigues, and W. P. dos Santos, "Early diagnosis of parkinson's disease using EEG, machine learning and partial directed coherence," *Research on Biomedical Engineering*, vol. 36, no. 3, pp. 311–331, 2020.
- [26] G. Wang, Z. Sun, R. Tao, K. Li, G. Bao, and X. Yan, "Epileptic seizure detection based on partial directed coherence analysis," *IEEE journal of biomedical and health informatics*, vol. 20, no. 3, pp. 873–879, 2015.
- [27] D. Chicharro, "On the spectral formulation of granger causality," *Biological cybernetics*, vol. 105, no. 5, pp. 331–347, 2011.
- [28] R. M. May, Simple mathematical models with very complicated dynamics. Springer, 2004.
- [29] D. Mønster, R. Fusaroli, K. Tylén, A. Roepstorff, and J. F. Sherson, "Causal inference from noisy time-series data — testing the convergent cross-mapping algorithm in the presence of noise and external influence," Future Generation Computer Systems, vol. 73, pp. 52 – 62, 2017.
- [30] N. Jackson, S. R. Cole, B. Voytek, and N. C. Swann, "Characteristics of waveform shape in parkinson's disease detected with scalp electroencephalography," *eneuro*, vol. 6, no. 3, 2019.
- [31] J. S. George, J. Strunk, R. Mak-McCully, M. Houser, H. Poizner, and A. R. Aron, "Dopaminergic therapy in parkinson's disease decreases cortical beta band coherence in the resting state and increases cortical beta band power during executive control," *NeuroImage: Clinical*, vol. 3, pp. 261–270, 2013.
- [32] M. F. Anjum, S. Dasgupta, R. Mudumbai, A. Singh, J. F. Cavanagh, and N. S. Narayanan, "Linear predictive coding distinguishes spectral EEG features of parkinson's disease," *Parkinsonism & Related Disorders*, vol. 79, pp. 79–85, 2020.
- [33] A. Singh, S. P. Richardson, N. Narayanan, and J. F. Cavanagh, "Mid-frontal theta activity is diminished during cognitive control in parkinson's disease," *Neuropsychologia*, vol. 117, pp. 113–122, 2018.
- [34] A. Singh, R. C. Cole, A. I. Espinoza, D. Brown, J. F. Cavanagh, and N. S. Narayanan, "Frontal theta and beta oscillations during lower-limb movement in parkinson's disease," *Clinical Neurophysiology*, vol. 131, no. 3, pp. 694–702, 2020.
- [35] [Online]. Available: https://narayanan.lab.uiowa.edu/article/datasets
- [36] F. Takens, "Detecting strange attractors in turbulence," in *Dynamical systems and turbulence, Warwick 1980*. Springer, 1981, pp. 366–381.
- [37] S. Ganguli and H. Sompolinsky, "Compressed sensing, sparsity, and dimensionality in neuronal information processing and data analysis," *Annual review of neuroscience*, vol. 35, pp. 485–508, 2012.
- [38] N. C. Swann, C. de Hemptinne, A. R. Aron, J. L. Ostrem, R. T. Knight, and P. A. Starr, "Elevated synchrony in parkinson disease detected with electroencephalography," *Annals of neurology*, vol. 78, no. 5, pp. 742– 750, 2015.
- [39] J. Zhang, M. J. Idaji, A. Villringer, and V. V. Nikulin, "Neuronal biomarkers of parkinson's disease are present in healthy aging," *NeuroImage*, vol. 243, p. 118512, 2021.
- [40] R. Gong, M. Wegscheider, C. Mühlberg, R. Gast, C. Fricke, J.-J. Rumpf, V. V. Nikulin, T. R. Knösche, and J. Classen, "Spatiotemporal features

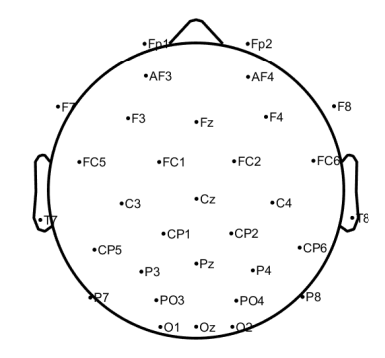
- of β - γ phase-amplitude coupling in parkinson's disease derived from scalp EEG," *Brain*, vol. 144, no. 2, pp. 487–503, 2021.
- [41] A. Fornito, A. Zalesky, and M. Breakspear, "The connectomics of brain disorders," *Nature Reviews Neuroscience*, vol. 16, no. 3, pp. 159–172, 2015
- [42] M. D. Fox, R. L. Buckner, H. Liu, M. M. Chakravarty, A. M. Lozano, and A. Pascual-Leone, "Resting-state networks link invasive and non-invasive brain stimulation across diverse psychiatric and neurological diseases," *Proceedings of the National Academy of Sciences*, vol. 111, no. 41, pp. E4367–E4375, 2014.
- [43] G. Rizzo, M. Copetti, S. Arcuti, D. Martino, A. Fontana, and G. Logroscino, "Accuracy of clinical diagnosis of parkinson disease," *Neurology*, vol. 86, no. 6, pp. 566–576, 2016.
- [44] L.-l. Gao and T. Wu, "The study of brain functional connectivity in parkinson's disease," *Translational neurodegeneration*, vol. 5, no. 1, pp. 1–7, 2016.
- [45] L. Sang, J. Zhang, L. Wang, J. Zhang, Y. Zhang, P. Li, J. Wang, and M. Qiu, "Alteration of brain functional networks in early-stage parkinson's disease: A resting-state fMRI study," *PLOS ONE*, vol. 10, no. 10, pp. 1–19, 10 2015.
- [46] A. Tessitore, M. Cirillo, and R. De Micco, "Functional connectivity signatures of parkinson's disease," *Journal of Parkinson's disease*, vol. 9, no. 4, pp. 637–652, 2019.
- [47] C. Gratton, J. M. Koller, W. Shannon, D. J. Greene, B. Maiti, A. Z. Snyder, S. E. Petersen, J. S. Perlmutter, and M. C. Campbell, "Emergent Functional Network Effects in Parkinson Disease," *Cerebral Cortex*, vol. 29, no. 6, pp. 2509–2523, 05 2018.
- [48] B. Klassen, J. Hentz, H. Shill, E. Driver-Dunckley, V. Evidente, M. Sabbagh, C. Adler, and J. Caviness, "Quantitative EEG as a predictive biomarker for parkinson disease dementia," *Neurology*, vol. 77, no. 2, pp. 118–124, 2011.
- [49] M. Chaturvedi, F. Hatz, U. Gschwandtner, J. G. Bogaarts, A. Meyer, P. Fuhr, and V. Roth, "Quantitative EEG (QEEG) measures differentiate parkinson's disease (PD) patients from healthy controls (HC)," Frontiers in Aging Neuroscience, vol. 9, 2017.
- [50] R. Yuvaraj, U. R. Acharya, and Y. Hagiwara, "A novel parkinson's disease diagnosis index using higher-order spectra features in EEG signals," *Neural Computing and Applications*, vol. 30, no. 4, pp. 1225– 1235, 2018.
- [51] C. Lainscsek, M. Hernandez, J. Weyhenmeyer, T. Sejnowski, and H. Poizner, "Non-linear dynamical analysis of EEG time series distinguishes patients with parkinson's disease from healthy individuals," *Frontiers in Neurology*, vol. 4, 2013.
- [52] O. Sporns, C. J. Honey, and R. Kötter, "Identification and classification of hubs in brain networks," *PLOS ONE*, vol. 2, no. 10, pp. 1–14, 10 2007. [Online]. Available: https://doi.org/10.1371/journal.pone.0001049
- [53] D. S. Bassett and E. T. Bullmore, "Small-world brain networks revisited," *The Neuroscientist*, vol. 23, no. 5, pp. 499–516, 2017, pMID: 27655008.
- [54] C. Wilke, G. Worrell, and B. He, "Graph analysis of epileptogenic networks in human partial epilepsy," *Epilepsia*, vol. 52, no. 1, pp. 84–93, 2011
- [55] M. M. Engels, C. J. Stam, W. M. van der Flier, P. Scheltens, H. de Waal, and E. C. van Straaten, "Declining functional connectivity and changing hub locations in alzheimer's disease: an EEG study," *BMC neurology*, vol. 15, no. 1, pp. 1–8, 2015.
- [56] H. Cheng, S. Newman, J. Goñi, J. S. Kent, J. Howell, A. Bolbecker, A. Puce, B. F. O'Donnell, and W. P. Hetrick, "Nodal centrality of functional network in the differentiation of schizophrenia," *Schizophrenia* research, vol. 168, no. 1-2, pp. 345–352, 2015.
- [57] H.-C. Baggio, R. Sala-Llonch, B. Segura, M.-J. Marti, F. Valldeoriola, Y. Compta, E. Tolosa, and C. Junqué, "Functional brain networks and cognitive deficits in parkinson's disease," *Human Brain Mapping*, vol. 35, no. 9, pp. 4620–4634, 2014.
- [58] S.-J. Lin, T. R. Baumeister, S. Garg, and M. J. McKeown, "Cognitive profiles and hub vulnerability in parkinson's disease," Frontiers in Neurology, vol. 9, 2018. [Online]. Available: https://www.frontiersin.org/article/10.3389/fneur.2018.00482
- [59] Y. Koshimori, S.-S. Cho, M. Criaud, L. Christopher, M. Jacobs, C. Ghadery, S. Coakeley, M. Harris, R. Mizrahi, C. Hamani, A. E. Lang, S. Houle, and A. P. Strafella, "Disrupted nodal and hub organization account for brain network abnormalities in parkinson's disease," Frontiers in Aging Neuroscience, vol. 8, 2016. [Online]. Available: https://www.frontiersin.org/article/10.3389/fnagi.2016.00259
- [60] T. Wu, J. Wang, C. Wang, M. Hallett, Y. Zang, X. Wu, and P. Chan, "Basal ganglia circuits changes in parkinson's disease patients," *Neuroscience letters*, vol. 524, no. 1, pp. 55–59, 2012.

- [61] T. R. Melzer, R. Watts, M. R. MacAskill, T. L. Pitcher, L. Livingston, R. J. Keenan, J. C. Dalrymple-Alford, and T. J. Anderson, "Grey matter atrophy in cognitively impaired parkinson's disease," *Journal of Neurology, Neurosurgery & Psychiatry*, vol. 83, no. 2, pp. 188–194, 2012.
- [62] A. B. Barrett, L. Barnett, and A. K. Seth, "Multivariate granger causality and generalized variance," *Physical Review E*, vol. 81, no. 4, p. 041907, 2010.
- [63] A. Bastos and J.-M. Schoffelen, "A tutorial review of functional connectivity analysis methods and their interpretational pitfalls," Frontiers in Systems Neuroscience, vol. 9, 01 2016.
- [64] Q. Liu, M. Ganzetti, N. Wenderoth, and D. Mantini, "Detecting large-scale brain networks using EEG: Impact of electrode density, head modeling and source localization," *Frontiers in neuroinformatics*, vol. 12, p. 4, 2018.
- [65] M. Beudel and P. Brown, "Adaptive deep brain stimulation in parkinson's disease," *Parkinsonism & related disorders*, vol. 22, pp. S123–S126, 2016

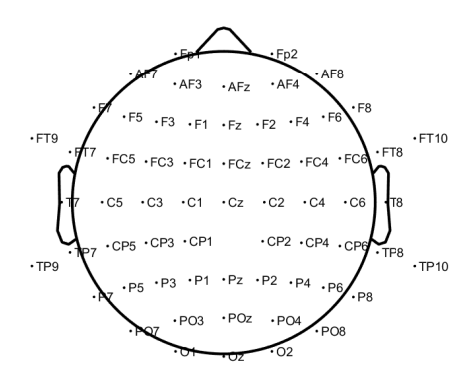
Supplementary Information: Effective Brain Connectivity Extraction by Frequency-Domain Convergent Cross-Mapping (FDCCM) and its Application in Parkinson's Disease Classification

Authors: Sandeep Avvaru and Keshab K. Parhi

S1 Scalp EEG Electrode Configuration



(a) PD Dataset-1



(b) PD Dataset-2

Figure S1: EEG channel locations plotted on a 2-D head diagram. Channels plotted beyond the head limit extend below the head center's horizontal plane. PD dataset-1 has 32 electrodes and PD dataset-2 has 63 electrodes.

S2 Classification Results Using Linear Support Vector Machines

Table S1: Summary of HC vs. PD classification results evaluated using leave-one-patient-out cross-validation scheme. The table presents classification accuracy, sensitivity (PD accuracy), specificity (HC accuracy) and AUC for each of the three network construction methods. Random label-assignment would result in a baseline accuracy of 50%. The highest values between the three methods are shown in bold.

	PD Dataset-1													
Classifier \rightarrow		HC vs	ΟN	HC vs. PD-OFF										
Connectivity ↓	Acc.	Sens.	Spec.	AUC (0-1)	Acc.	Sens.	Spec.	AUC (0-1)						
Correlation	83.87	100.00	68.75	0.82	77.42	80.00	75.00	0.70						
CCM	70.97	60.00	81.25	0.74	74.19	80.00	68.75	0.70						
FDCCM	74.19	60.00	87.50	0.62	77.42	86.67	68.75	0.80						
	PD Dataset-2													
Correlation	72.22	55.56	88.89	0.68	70.37	55.56	85.19	0.69						
CCM	70.37	51.85	88.89	0.68	77.78	62.96	92.59	0.75						
FDCCM	77.78	85.19	70.37	0.84	77.78	70.37	85.19	0.79						

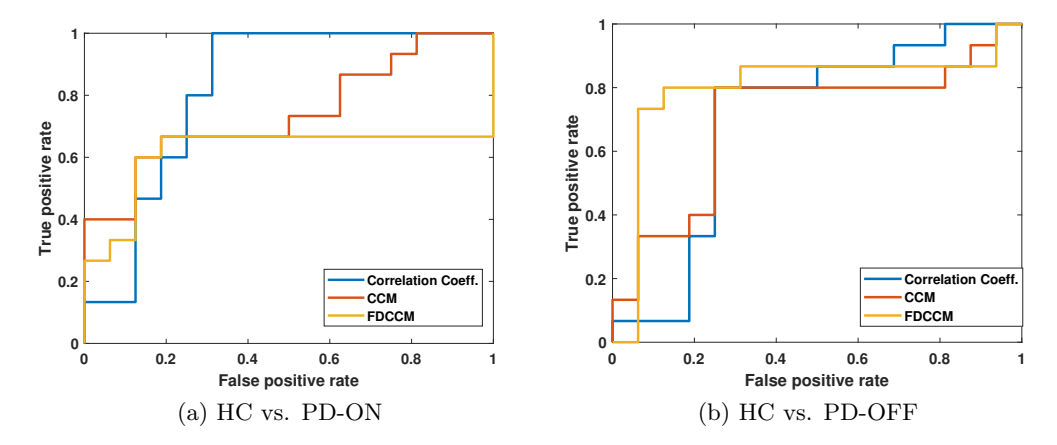


Figure S2: HC vs. PD receiver operating characteristic (ROC) curves - PD dataset-1.

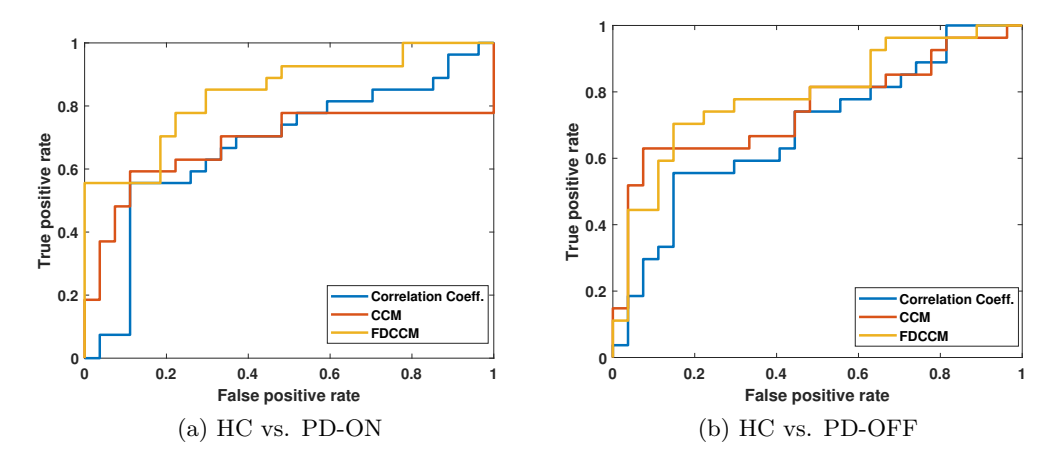


Figure S3: HC vs. PD receiver operating characteristic (ROC) curves - PD dataset-2.

S3 Classification Results Using Linear Discriminant Analysis

Table S2: Summary of HC vs. PD classification results evaluated using leave-one-patient-out cross-validation scheme. The table presents classification accuracy, sensitivity (PD accuracy), specificity (HC accuracy) and AUC for each of the three network construction methods. Random label-assignment would result in a baseline accuracy of 50%. The highest values between the three methods are shown in bold.

PD Dataset-1													
Classifier \rightarrow		HC v	s. PD-	ON	HC vs. PD-OFF								
Connectivity ↓	Acc.	Sens.	Spec.	AUC (0-1)	Acc.	Sens.	Spec.	AUC (0-1)					
Correlation	77.42	60.00	93.75	0.74	74.19	73.33	75.00	0.66					
CCM	64.52	46.67	81.25	0.57	77.42	93.33	62.50	0.75					
FDCCM	77.42	93.33	62.50	0.60	77.42	93.33	62.50	0.63					
	PD Dataset-2												
Correlation	74.07	74.07	74.07	0.74	74.07	62.96	85.19	0.70					
CCM	72.22	51.85	92.59	0.71	68.52	51.85	85.19	0.65					
FDCCM	68.52	92.59	44.44	0.60	68.52	77.78	59.26	0.68					

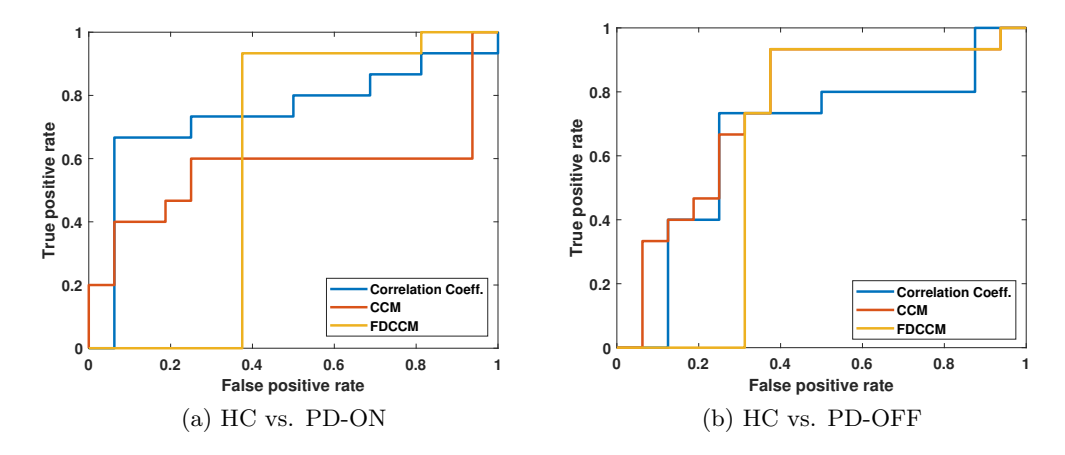


Figure S4: HC vs. PD receiver operating characteristic (ROC) curves - PD dataset-1.

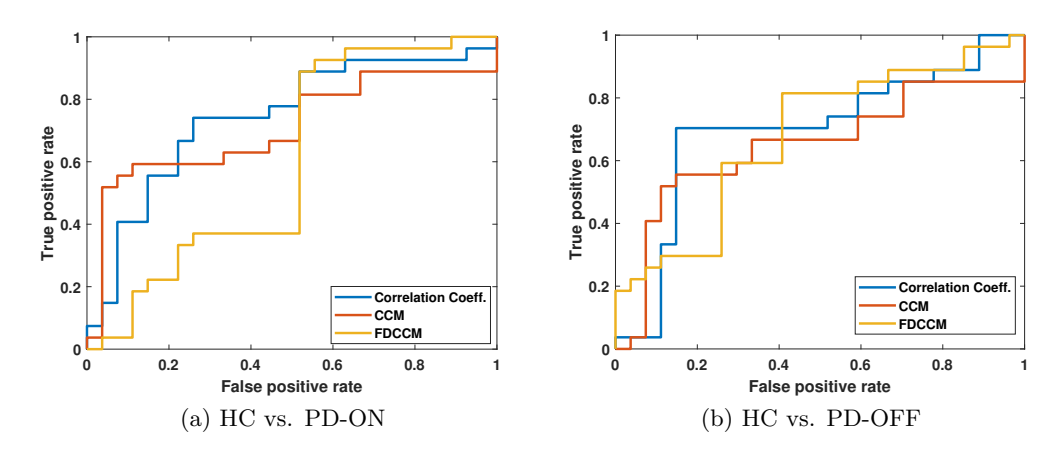


Figure S5: HC vs. PD receiver operating characteristic (ROC) curves - PD dataset-2.

S4 Classification Results Using Radial Basis Function Kernel Support Vector Machines (RBF-SVM)

Table S3: Summary of HC vs. PD classification results evaluated using leave-one-patient-out cross-validation scheme. The table presents classification accuracy, sensitivity (PD accuracy), specificity (HC accuracy) and AUC for each of the three network construction methods. Random label-assignment would result in a baseline accuracy of 50%. The highest values between the three methods are shown in bold.

PD Dataset-1													
Classifier \rightarrow		HC v	s. PD-	ON	HC vs. PD-OFF								
Connectivity \$\dpressure\$	Acc.	Sens.	Spec.	AUC (0-1)	Acc.	Sens.	Spec.	AUC (0-1)					
Correlation	70.97	86.67	56.25	0.53	70.97	40.00	100.00	0.40					
CCM	74.19	60.00	87.50	0.71	77.42	53.33	100.00	0.69					
FDCCM	80.65	86.67	75.00	0.83	80.65	73.33	87.50	0.90					
	PD Dataset-2												
Correlation	72.22	92.59	51.85	0.60	72.22	70.37	74.07	0.72					
CCM	75.93	77.78	74.07	0.65	77.78	66.67	88.89	0.66					
FDCCM	70.37	59.26	81.48	0.74	72.22	70.37	74.07	0.74					

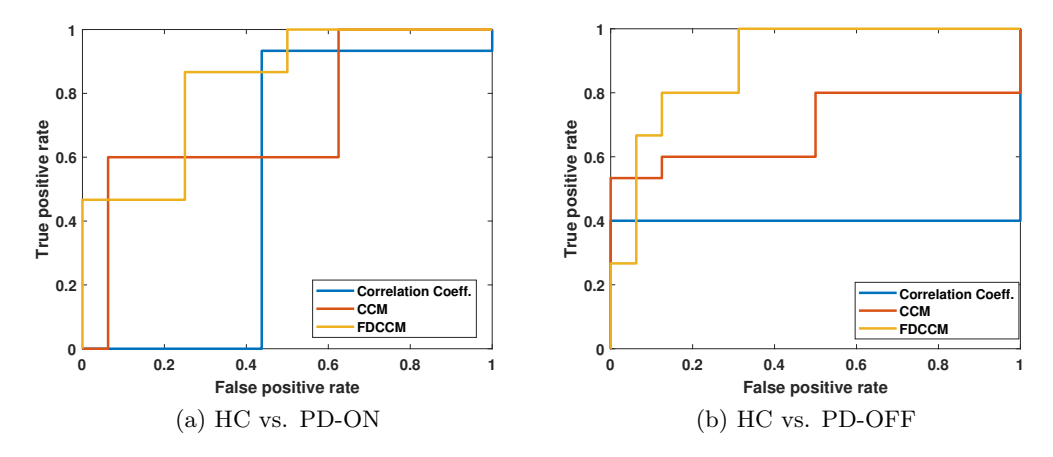


Figure S6: HC vs. PD receiver operating characteristic (ROC) curves - PD dataset-1.

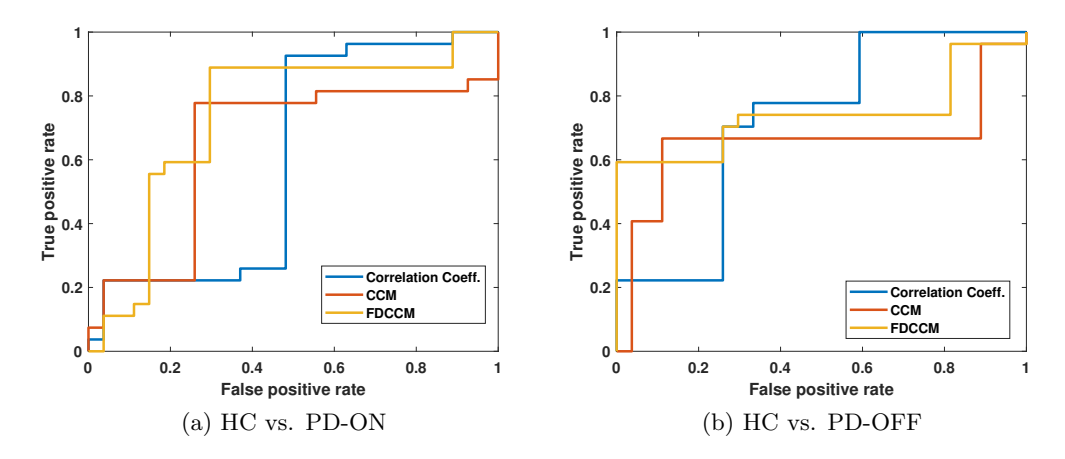


Figure S7: HC vs. PD receiver operating characteristic (ROC) curves - PD dataset-2.

S5 Classification Results Using Decision Trees

Table S4: Summary of HC vs. PD classification results evaluated using leave-one-patient-out cross-validation scheme. The table presents classification accuracy, sensitivity (PD accuracy), specificity (HC accuracy) and AUC for each of the three network construction methods. Random label-assignment would result in a baseline accuracy of 50%. The highest values between the three methods are shown in bold.

PD Dataset-1													
Classifier \rightarrow		HC v	s. PD-	ON	HC vs. PD-OFF								
Connectivity ↓	Acc.	Sens.	Spec.	AUC (0-1)	Acc.	Sens.	Spec.	AUC (0-1)					
Correlation	77.42	80.00	75.00	0.63	77.42	73.33	81.25	0.74					
CCM	77.42	66.67	87.50	0.68	87.10	86.67	87.50	0.81					
FDCCM	80.65	86.67	75.00	0.78	90.32	86.67	93.75	0.85					
	PD Dataset-2												
Correlation	72.22	92.59	51.85	0.60	72.22	70.37	74.07	0.72					
CCM	75.93	77.78	74.07	0.65	77.78	66.67	88.89	0.66					
FDCCM	70.37	59.26	81.48	0.74	72.22	70.37	74.07	0.74					

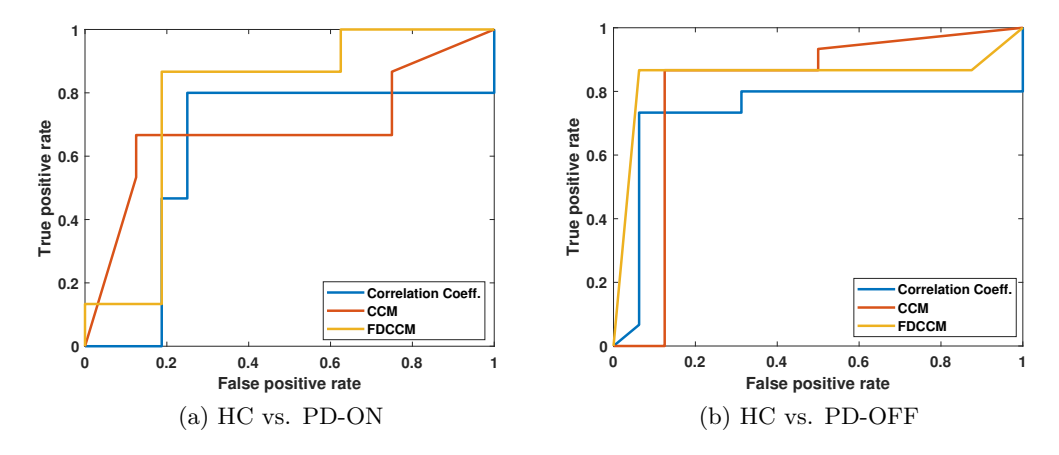


Figure S8: HC vs. PD receiver operating characteristic (ROC) curves - PD dataset-1.

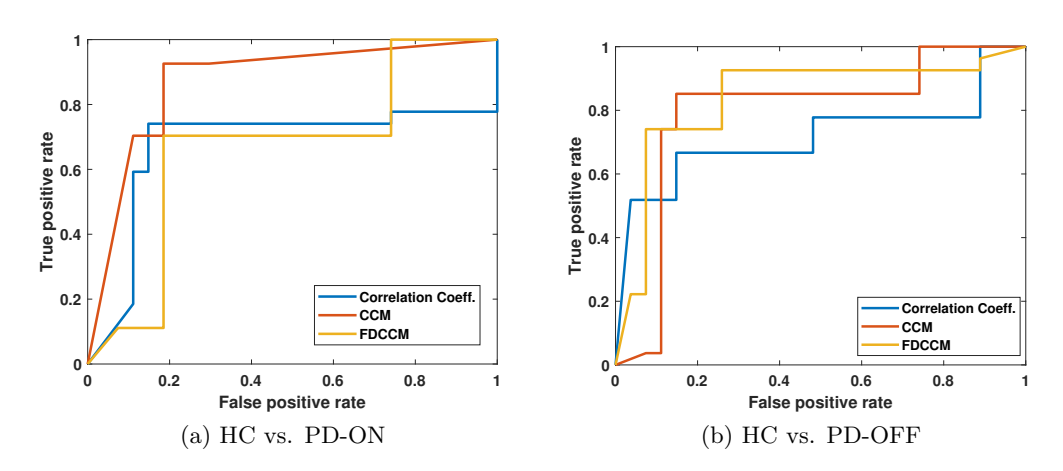


Figure S9: HC vs. PD receiver operating characteristic (ROC) curves - PD dataset-2.

S6 Classification Results Using signals limited to 50 Hz and 100 Hz

Table S5: Summary of HC vs. PD region-level classification results evaluated using leave-one-patient-out testing using filtered data up to 50 Hz and 100 Hz from dataset-1. All classifiers were trained using decision trees with left-temporal lobe features. The table presents classification accuracy, sensitivity (PD accuracy), specificity (HC accuracy) and AUC for each of the three network construction methods. Random label-assignment would result in a baseline accuracy of 50%. The highest values between the three methods are shown in bold.

PD Dataset-1													
Classifier \rightarrow		cutof	f at 50	Hz	cutoff at 100 Hz								
Connectivity ↓	Acc.	Sens.	Spec.	AUC (0-1)	Acc.	Sens.	Spec.	AUC (0-1)					
Correlation	51.61	46.67	56.25	0.43	45.71	33.33	55.00	0.33					
CCM	58.06	60.00	56.25	0.50	52.78	33.33	66.67	0.36					
FDCCM	77.42	86.67	68.75	0.63	75.00	73.33	76.19	0.69					